Journal of Materials Chemistry B

Accepted Manuscript

ROYAL SOCIETY OF CHEMISTRY

www.rsc.org/materialsB

Promoting bone-like apatite formation on titanium alloys through nanocrystalline tantalum nitride coatings

Jiang Xu[a,b*], Linlin Liu[a], Paul Munroe[c], Zong-Han Xie[d,e*]

a. Department of Material Science and Engineering, Nanjing University of Aeronautics and Astronautics, 29 Yudao Street, Nanjing 210016, PR China

b. School of Mechanical & Electrical Engineering, Wuhan Institute of Technology, 693 Xiongchu Avenue, Wuhan, 430073,P. R. China

c. School of Materials Science and Engineering, University of New South Wales, NSW 2052, Australia

d. School of Mechanical Engineering, University of Adelaide, SA 5005, Australia

e. School of Engineering, Edith Cowan University, WA 6027, Australia

Abstract:

The study aims to advance the applicability of titanium alloys as bone implant materials by tackling some important aspects of surface robustness and bioactivity. To do so, biologically active Ta-N nanocrystalline coatings were engineered on Ti–6Al–4V alloy substrates by reactive sputter deposition using a double glow discharge plasma technique. The surface morphology, phase composition and structure of the coatings were characterized by using atomic force microscopy (AFM), X-ray diffraction (XRD), X-ray photoelectron spectroscopy (XPS), scanning electron microscopy (SEM) and transmission electron microscopy (TEM). The newly developed coatings are extremely dense, adherent and composed of cubic TaN phase and a minor fraction of hexagonal Ta_2N phase. The microstructure of Ta-N coatings consists of nanocrystallites of about 15–20 nm in diameter, having a strong TaN (200)-oriented texture. Moreover, the coatings exhibit a uniform nanopillar structure on the surface, critical for the observed bioactivity. Scratching tests were undertaken to evaluate the adhesion strength between the Ta-N coatings and Ti-6Al-4V alloy substrates. The Ta-N coatings were found to exhibit a high scratch resistance and are thus suitable for load-bearing applications. The apatite-inducing ability of the coatings was evaluated *in vitro* using a simulated body fluid (SBF) that has almost equal compositions of inorganic ions to human blood plasma. After soaking in the solution for up to 14 days, only a few apatite particulates were observed on the surface of untreated Ti-6A1-4V alloy. By contrast, the surface of the Ta-N

*Corresponding authors.
E-mail addresses: xujiang73@nuaa.edu.cn (J. Xu), zonghan.xie@adelaide.edu.au(Z.-H. Xie).

coatings was completely covered by a compact, AB-type apatite layer free of micro-cracks. High resolution transmission electron microscopy (HRTEM) observations reveal that after soaking for 14 days, the apatite layer, formed through a biomimetic process, comprises closely packed, needle-shaped apatite crystals of 34.5±12.4 nm in length and 6.0±0.2 nm in width. Moreover, nanotwins were identified in apatite, reminiscent of those found in bone minerals. The negatively-charged surface, combined with unique surface structure of the Ta-N nanoceramic coatings, is believed to be responsible for the formation of homogenous, compact bone-like apatite layer. The Ta-N nanoceramic coatings are expected to find applications as an integral part of biomaterials used in bone repair and replacement.

Keywords: Nanocrystalline coatings; Tantalum nitrides; Apatite crystals; Simulated body fluid; Biomimetic process.

1. Introduction

Titanium alloys such as Ti-6Al-4V are among the most widely used load-bearing biomedical metals for bio-implant applications, due to a desirable combination of biocompatibility, mechanical properties and corrosion resistance [**1, 2**]. An essential requirement for successful orthopedic implanted materials to achieve rapid osseointegration is dependent on the formation capability of a biologically active bone-like apatite layer between the implant and bone, when embedded in living body [**3, 4**]. Unfortunately, Ti alloys are generally expected to be bioinert with biological systems in the human body. Consequently, implants made of Ti alloys used in bone reconstruction are merely encapsulated by a fibrous tissue and become isolated from the surrounding bone, leading to the osteolysis and subsequent loosening of implants [**5, 6**]. Moreover, the metal ions released from Ti alloy implant due to its frequent interactions with the surrounding physiological environment can inflict a myriad of detrimental effects on the health of patients in long term [**1, 7, 8**].

It is understood that the surface properties play a critical role in the stability and function of bone-rebuilding materials. Over the past decades considerable effort has been devoted to modify the surface characteristics of Ti alloys by introducing various bioactive coatings, for example, those made of sodium titanate and bioactive hydroxyapatite (HA), by using different surface

treatment methods [**6, 9-12**]. It is well known that the functions of deposited films are strongly affected by their microstructure, surface roughness and morphology, crystalline structure and chemical composition, as well as their adhesion to metallic implants [**13**]. Although coated Ti alloys have shown the potential to induce apatite formation, there remain some serious problems to be resolved. For example, plasma-sprayed HA coatings possess several undesirable properties that are adverse to prolonged use in the living body, since these coatings contain large numbers of molten particles, porosities and cracks [**14, 15**]. Furthermore, the large mismatch in the coefficient of thermal expansion (CTE) between the hydroxyapatite coating and the metal substrate could lead to catastrophic failure at the coating/substrate interface [**16**]. On the other hand, the sodium ions are easily released from the sodium titanate inside the body after implant surgery, which compromises apatite-forming ability of the alkali-treated Ti metals [**17, 18**]. Therefore, there is urgent need to develop new coatings that are strong, adherent and bioactive — promoting the growth of high quality bone-like apatite layer on the surface of implant alloys.

Due to its unique chemical and physical properties, tantalum nitride has attracted much attention in a variety of engineering applications, such as diffusion barrier layers in integrated circuits [**19**], hard wear-resistant coatings for cutting tools [**20**], and stable thin film resistors [**21**]. In addition to these industrial usages, tantalum nitride based materials (for instance, TaN, Ta_2N and TaC_xN_{1-x}) are biocompatible and, serving as protective coatings, they are being tested in an attempt to replace low-temperature isotropic pyrolytic carbon (LTIC) in the manufacture of durable artificial heart valves [**22, 23**]. Despite its potential for load-supporting implant applications [**24**], to date, there have been no reports with regard to the osteoconductive properties of tantalum nitrides.

In the present study, biologically active Ta-N nanocrystalline coatings were deposited onto Ti-6A1-4V alloy substrates by reactive sputter-deposition inside a double cathode glow discharge apparatus. Following the composition, microstructure and micro-scratching analysis of these Ta-N coatings, the *in vitro* bioactivity of the nanoceramic coatings was evaluated by soaking the specimens in a simulated body fluid (SBF) with ion concentrations mimicking those found in human blood plasma for up to 14 days. To obtain an in-depth understanding of apatite formation mechanism, the surface morphology, chemical composition and structure of the coatings after soaking in SBF for different periods of time were characterized by SEM equipped with

energy-dispersive X-ray analysis (EDX), X-ray diffraction (XRD), transmission electron microscopy (TEM), and Fourier transform infrared spectroscopy (FT-IR). Supported by this work, nanocrystalline Ta-N coatings should find applicability as robust, bioactive surfaces on metal implants for bone repair.

2. Materials and methods

2.1. Coating specimen preparation

Disk-shaped substrate specimens in size of Φ 40×3 mm were cut from a medical grade Ti-6Al-4V alloy bar. The nominal composition of this alloy in wt.% is given as: Al, 6.42; V, 4.19; Fe, 0.198; O, 0.101; C, 0.011; N, 0.006; and the balance, Ti. Before sputter deposition, the substrates were ground and then polished consecutively with silicon carbide papers down to 1200 grits, followed by cleaning with pure acetone and distilled water in a ultrasonic bath. Tantalum nitride (Ta-N) coatings were deposited onto polished Ti-6Al-4V substrates by using a double cathode glow discharge apparatus. A 99.99% pure Ta disk with a diameter of 100 mm and thickness of 5 mm was used as sputtering target. During the process of sputter-deposition, one cathode was the target composed of the desired sputtering material, and the other was the substrate. When voltages were applied to the two cathodes, glow discharge occurred, as described elsewhere [**25**]. The base pressure in the chamber was evacuated to 5×10^{-4} Pa to avoid the contamination in the coating process. The working pressure was set at 35 Pa consisting of Ar and N_2 gas mixture, with an Ar:N_2 flux ratio of 10:1. Using orthogonal test design, deposition parameters for the coatings were optimized and are given as follows: target electrode bias voltage with direct current, -850 V; substrate bias voltage with impulse current, -250 V; substrate temperature, 800 ℃; target/substrate distance, 10 mm; and treatment time, 1.5 h.

2.2 Scratching tests

The adhesion strength between the Ta-N coatings and Ti-6Al-4V alloy substrates was estimated by using a scratch tester (WS-97), equipped with an acoustic emission (AE) detector. The scratch tests were performed by drawing a Rockwell C diamond indenter of 200 μm in radius across the coatings surfaces under a normal load increasing linearly from 0 to 100 N. The loading rate was set at 20 N/min and the scratch speed was 1 mm/min. An AE sensor was attached near the

diamond indenter tip to detect the acoustic signals emitted from the coating damage. The minimum load at which a sudden increase in the intensity of the acoustic signals occurs is commonly defined as the critical load (L_c) that represents the coating adhesion strength.

2.3. Apatite formation in SBF

The apatite forming ability of the coated and uncoated specimens was evaluated by soaking them in 40 ml of simulated body fluid (SBF) with ion concentrations (Na^+ 142.0, K^+ 5.0, Mg^{2+} 1.5, Ca^{2+} 2.5, Cl^- 147.8, HCO_3^- 4.2, HPO_4^{2-} 1.0, SO_4^{2-}0.5 mM) similar to those of human blood plasma at 36.5 ℃. The SBF solution was prepared according to the composition and procedures described by Kokubo and Takadama [**26**]: Regent-grade chemicals of NaCl, $NaHCO_3$, KCl, $K_2HPO_4{\cdot}3H_2O$, $MgCl_2{\cdot}6H_2O$, $CaCl_2$ and Na_2SO_4 were dissolved in double-distilled water and buffered at pH 7.4 with tris-hydroxymethyl aminomethane ($(CH_2OH)_3CNH_2$) and 1 M hydrochloric acid (HCl). To keep the ion concentration stable, the SBF solution was refreshed every 2 days. After being soaked for predetermined intervals (i.e., 2, 7 and 14 days), the specimens were removed from the solution, then washed gently with pure water, before being dried in a vacuum desiccator for subsequent analysis. The changes in the pH value of SBF solutions were monitored by using a pH meter (NIST standards, Oakton).

2.4. Materials characterization

The surface morphologies of specimens were analyzed by atomic force microscopy (AFM, Veeco Nanoscope V) equipped with NanoScope imaging software (Digital Instruments, Inc.). An area of 1 μm × 1 μm was scanned under contact mode with tip NSC36 and scan rate 1.0 Hz for each measurement. Several topographic images were collected for each of the tested samples at different locations to evaluate surface roughness. Average surface roughness (R_a) values were determined to determine the change of surface roughness of specimens before and after sputter deposition.

Phase identification of the as-deposited coatings was characterized by X-ray diffraction (XRD) using D8 ADVANCE diffractometer with a Cu K_α irradiation (λ = 0.154060 nm) operating at 35 kV and 40 mA. X-ray spectra were collected in the scanning angle ranging from 20 to 100° with a step rate of 0.05° s^{-1}. The as-deposited coatings was etched with the use of Kroll's reagent (10 ml

HNO_3, 4 ml HF and 86 ml H_2O) for 15-25 s to obtain a good visibility of the coating/substrate interface. The surface morphologies and chemical composition of the as-deposited Ta-N coatings, before and after SBF-soaking, were observed by field emission scanning electron microscopy (FESEM; Hitachi, S-4800, Japan) equipped with an energy-dispersive X-ray analyzer (EDX-4; Philips).

Transmission electron microscopy (TEM) was performed using a JEOL JEM-2010 microscope operated with an accelerating voltage of 200 kV. For the TEM plan-view of the coating microstructure, the specimens were prepared by cutting, grinding, dimpling and single-jet electropolishing from the untreated side of the substrate. To prepare TEM powder sample, the ultrasound vibration technique was employed [**27**] and can be described as follows: After SBF soaking, the sample covered by an apatite layer was immersed in ethanol solution and ultrasound vibration was applied to separate the apatite precipitates from the substrate. The precipitates were then carefully extracted from the solution and picked up using TEM copper grids covered with carbon films.

Before and after SBF-soaking, the surface chemistry of the Ta-N coatings was analyzed by X-ray photoelectron spectroscopy (XPS) using a Kratos AXIS Ultra ESCA System containing an Al Kα X-ray source with an energy of 1486.6 eV. The accelerating voltage and emission current of the X-ray source were kept at 12 kV and 12 mA, respectively. The base pressure of the sample analysis chamber was maintained at ~10^{-10} Torr. The pass energy was selected at 80 eV for survey scans and 10 eV for the feature scans to ensure high resolution and good sensitivity. After subtracting the background signal, the spectra were fitted by both Gaussian and mixed Gaussian/Lorentzian functions. Peak positions were then calibrated with respect to the C1s peak at 284.8 eV from the hydrocarbon contamination. Peak identification was performed by reference to the NIST XPS database (V4.0). Furthermore, fourier transform infrared spectroscopy (FT-IR, Nicolet-870, USA) was used to ascertain what types of the apatite crystals formed on the sample surface after immersion in SBF. The FT-IR spectra were measured in transmittance mode using the KBr technique in the range from 4000 to 400 cm^{-1} at a resolution of 2 cm^{-1}.

3. Results

3.1 Coating microstructural characterization

Surface morphologies of the polished Ti-6Al-4V alloy before and after sputter deposition are displayed in **Fig. 1(a)** and **(b)**. The Ta-N nanoceramic coating exhibits nanopillar structures, with each pillar having a height of 29.4±2.4 nm and a diameter of 23.0±1.4 nm. In contrast, the polished Ti-6Al-4V alloy has a smooth surface. The average surface roughness (R_a) values increased from 1.2 nm for the polished Ti-6Al-4V alloy to 6.9 nm after sputter deposition.

Fig. 1(c) shows the X-ray diffraction pattern of the Ta-N coatings prepared onto Ti-6Al-4V alloy substrates obtained by reactive sputtering at an Ar : N_2 flux ratio of 10 : 1. The overwhelmingly strong and broad diffraction peak located at $2\theta = 41.4^{\circ}$ can be assigned to the (200) reflection of face-centered cubic (fcc) TaN (JCPDS No. 49-1283), whereas the intensity of diffraction peaks arising from other reflection planes, such as (220), (331) and (400), is very weak, indicating that the Ta-N coatings possess a preferred TaN (200) orientation. Tsukimoto *et al.* found that the preferred orientation of TaN films is very sensitive to the gas flow ratio of N_2 vs. Ar during sputter-deposition, and that (200) preferred orientation became stronger with increasing N_2 flow rate [**19**]. In addition, weak diffraction peaks originating from hexagonal Ta_2N (JCPDS No. 26-0985) can be detected, implying that the Ta-N coating is composed of fcc-TaN phase and a minor fraction of Ta_2N phase. The theoretical analysis suggests that in the Ta-N system Ta_2N and TaN phase have stable and metastable structures, respectively, and that the energy difference calculated for these two tantalum nitrides is very close [**28**]. It is understood that kinetic factors, closely related to coating deposition conditions, such as the diffusion barriers for atomic rearrangement and epitaxial stabilization effects, played an important role in generating final phase compositions of deposited coatings, thus partly responsible for the coexistence of Ta_2N and TaN phases in the Ta-N coatings.

A typical FE-SEM cross-sectional view of the sputter-deposited Ta-N coatings is shown in **Fig. 1(d)**. Notably, the Ta-N coatings exhibit an extremely dense and homogeneous structure with a thickness of ~30 μm, and appears to be well adhered to the Ti-6Al-4V alloy substrates. Generally speaking, ceramic coatings having a dense structure would crack or peel off if the thickness reaches a threshold value (usually less than 10 μm), mainly due to internal stresses induced by both energetic particle bombardment and thermal expansion mismatch between the coating and substrate [**29**]. Surprisingly, the Ta-N nanoceramic coatings prepared by the reactive sputtering process employed in this work are ultra-thick and of good quality. This may be attributed to the

high deposition temperature, compared with other deposition techniques [**30**]. High deposition temperature is believed to bring two benefits for the coating growth: a) it increase the mobility of the atoms deposited on the substrate, allowing the atoms to diffuse across the surface and to overcome self-shadowing effect exerted by previously deposited atoms, and b) release the internal stresses in the growing coatings. Because of its barrier effect, a thicker Ta-N ceramic coating would provide greater mechanical protection and increase the corrosion resistance in the body environment.

A plane-view TEM bright-field image of the as-deposited Ta-N ceramic coatings is shown in **Fig. 1(e)** with corresponding selected area electron diffraction (SAED) pattern. The Ta-N ceramic coatings are composed of nanocrystallites of about 15–20 nm in diameter. An intense TaN (200) ring in the SAED pattern indicates that the coatings exhibit a strong TaN (200)-oriented texture, which is in agreement with the XRD results. A bright-field HRTEM lattice image (**Fig. 1(f)**) shows that the spacing of the lattice fringes within two dotted circles (seen as A and B in the figure) are calculated as 2.15 and 1.32 Å, which correspond to the (200) and (311) lattice planes of fcc-TaN, respectively.

In order to further reveal the phase composition of the as-deposited Ta-N coatings, the chemical bonding states of the coatings were probed by the X-ray photoelectron spectroscopy (XPS). **Fig. 2(a)** presents the Ta 4f core-level spectra recorded from the as-deposited Ta-N coatings before and after 10 min of sputtering with a 4.5 kV Ar^+ ion beam. The Ta 4f spectrum was reported to consist of both the Ta$4f_{7/2}$ and the Ta $4f_{5/2}$ photoelectron lines with a theoretical Ta $4f_{7/2}$/Ta $4f_{5/2}$ area ratio of 4:3 and a spin-orbit splitting of 1.9 eV [**31**]. The broad Ta 4f spectrum of the unsputtered Ta-N coatings, originating from different chemical species, can be deconvoluted into three well separated doublets. The low energy sides of two doublets with binding energy of Ta $4f_{7/2}$ located respectively at 22.7 and 23.3 eV are assigned to Ta_2N and TaN [**32**], while one high-energy-side doublet with binding energy of Ta $4f_{7/2}$ at 26.1 eV accords with the chemical state of Ta in the form of TaO_xN_y [**33**]. By quantitative analysis of the XPS data, the phase fractions (at.%) for the Ta-N coatings are derived, i.e., 23.4% Ta_2N , 65.2% TaN and 11.4% TaO_xN_y, respectively.

As for the samples subjected to 10 min of sputtering, the Ta 4f spectra shift to higher binding energies by about ~0.2 eV as compared to the unsputtered samples and, moreover, the Ta 4f

doublet corresponding to TaO_xN_y disappears. The shift in the core level may be due to the structure damage caused by the sputtering. The XPS results also suggest that tantalum oxynitride was formed from the partial oxidation of the Ta-N ceramic coatings when the sample was removed from the sputtering system and exposed to ambient air atmosphere. This phenomenon was also observed by other researchers [**34, 35**].

3.2. Scratching tests

Scratch resistance is routinely used to define the adhesion strength between the as-deposited coating and the substrate, which also reflects the load bearing capacity, fracture toughness and wear resistance of a coating [**36-38**]. The acoustic emission signals are plotted as a function of the normal load in **Fig. 2(b)**. First acoustic emission peak was detected when the scratching load reached 60 N, and thus the critical load at which the coating delamination occurred, is 60 N. Note, this value is much greater than that of tantalum nitride films (12-28 N) formed on Ta substrate synthesized by reactive magnetron sputtering [**22**]. As a general rule, a critical load of above 30 N measured with a Rockwell C diamond tip in scratch testing is believed to be sufficient for sliding contact applications [**39**]. Therefore, the Ta-N coatings are suitable for load-bearing applications.

3.3. Apatite-inducing ability

3.3.1. SEM observation

Apatite-inducing ability of a material in SBF *in vitro* is frequently used to predict the *in vivo* bioactivity of the material [**26**]. **Fig. 3** displays the characteristic surface morphologies of the uncoated and Ta-N coated Ti-6Al-4V samples after being soaked in SBF for different periods of time. As shown in **Fig. 3(a)** and **(b)**, the uncoated Ti-6Al-4V alloy surface showed no visible (2 days) or a few apatite precipitates (7 days) after soaking in SBF. After 2 weeks of SBF soaking, only a small amount of loose apatite clusters with an irregular morphology formed and scattered sparsely on the surface of the uncoated Ti-6Al-4V alloy (**Fig.3(c)**). EDS analysis (upper inset in **Fig.3(c)**) showed that O, Ca and P were highly enriched in these precipitates with a Ca/P molar ratio of 1.03, indicative of some sort of calcium phosphate compound mineralized from SBF.

By contrast, for the Ta-N nanoceramic coatings, almost the entire surface was coated by

numerous floccule-like particulates after soaking in SBF for 2 days (**Fig. 3(d)**). As can be seen from **Fig. 3(e)**, after 7 days of immersion, the surface of the coatings was completely covered with a homogeneous and compact apatite-like layer, consisting of overlapping spheroidal particles of about 1~2 μm in diameter tightly packed together. Such apatite spherulites were quite similar to that of the TiO_2-coated titanium after 3 days immersion in phosphate buffered saline (PBS) [**40**]. With a further increase in soaking time to 14 days, the surface morphology of the apatite-like layer was found to be denser and smoother, comprising elongated nano-sized fibers (inset in **Fig. 3(f)**).

It is important to note that, irrespective of the SBF compositions used, micro-cracks are oftentimes present in the biomimetic deposition of apatite layers, which has been documented in a large number of publications and remains a challenging issue [**41-43**]. These cracks could lead to degradation and delamination of apatite layers formed on the implant surface. However, as shown in **Fig. 3(f)**, the crack-free apatite layer has grown on the Ta-N nanoceramic coatings, which would reduce the chance of delamination, thereby increasing the bond strength between the bone material and metallic implants [**44**]. The upper right insets in **Fig. 3(d)-(f)** present representative EDS spectrum recorded from the precipitated apatite layers on the Ta-N nanoceramic coatings with different soaking times in SBF. Chemical composition obtained from each sample were measured at five different regions with a 15 μm × 15 μm scan area in each measurement. It can be seen from **Fig. 3(g)** that after 2 days of exposure in SBF, the atomic ratio of Ca to P of the apatite layers was found to be 1.16±0.07, and then increased to 1.42±0.04 after 7 days of immersion. Finally, after 14 days of immersion, the Ca/P ratio reached 1.62±0.02, which is close to the stoichiometric value of 1.67 for hydroxyapatite (HA, $Ca_{10}(PO_4)_6(OH)_2$). Furthermore, the intensity of Ta peaks obtained from underneath the Ta-N nanoceramic coatings diminished drastically, denoting that the thickness of the apatite layers increased accordingly.

3.3.2. TEM observation

To elucidate the mechanism governing the nucleation and growth of apatite layers, the morphology, crystal structure and orientation of apatite layers grown on the Ta-N nanoceramic coatings were examined in great details using analytical and high-resolution TEM (HRTEM). **Fig. 4** shows TEM image of as-received apatite formed on the Ta-N nanoceramic coatings after 2, 7 and 14 days of soaking in SBF. As shown in **Fig. 4(a)** and **(b)**, after 2 days of soaking, apatite

precipitates exhibit a typical amorphous structure, as evidenced by a diffused halo in the SAED pattern and a featureless contrast in bright field HRTEM image. The calcium phosphate with amorphous structure usually has a low Ca/P molar ratio [**45**], which is in agreement with the EDS results shown in **Fig. 3**. During the initial stage of apatite construction, the formation of amorphous calcium phosphate was preferred, due to a lower energy barrier for nucleation, as compared to its crystalline counterpart [**46**]. Some bright circular spots can also been seen, as indicated by arrows in **Fig. 4(a)**. Presumably, they arose from irradiation damage from electron beam, since the amorphous calcium phosphate is a metastable phase under electron beam. Similar irradiation phenomenon was also observed on the surface of apatite platelets formed on polystyrene substrates immersed in SBF with pH=6.5 [**47**].

As seen from **Fig. 4(c)**, after 7 days of soaking, apatite deposit exhibits a nanocomposite structure, comprising nanocrystallites (darker contrast) with an average size of ~6 nm in diameter, homogenously embedded in an amorphous matrix. Two resolvable crystallites are marked with red circles in **Fig. 4(d)**, and the spacing of the lattice fringes were calculated as 0.285 nm by fast Fourier transformation (FFT) analysis, which corresponds to the interplanar distance of the (211) plane of HA. This can be confirmed by the brightest diffraction ring in the SAED pattern identified as the (211) plane of HA. After soaking for 14 days, a low magnification image reveals that the apatite precipitates were agglomerates of needle-like crystals of 34.5±12.4 nm in length and 6.0±0.2 nm in width. As shown in **Fig. 4(f)**, the lattice fringe images of individual needles are identical, implying that these needles single crystals. Two appreciable diffraction rings can be assigned to (002) and (211) of planes of HA, respectively, giving rise to the lattice d-spacing values of 0.346 nm and 0.820 nm correspondingly. SAED pattern also reveals the presence of (002) plane arcs, demonstrating the preferential alignment of HA crystals in the precipitates. The high-resoluton TEM image (**Fig. 4(g)**) indicates that the longitudinal direction of each needle is parallel to the c axis ((002) plane direction) of the hexagonal hydroxyapatite structure and its transverse direction is parallel to the direction of (100) plane of HA. The angle between the two directions of 88.7° measured from the lattice fringes in **Fig. 4(g)** is very close to the calculated angle of 90°.

From the point of view of the energy barrier, the nucleation and growth of needle-shaped apatite is desirable, because the plane parallel to the c axis of apatite single crystals has a lower

surface energy, compared to other planes [**48**]. It is worth noting that the morphology, size and orientation of needle-shaped HA single crystals produced by the biomimetic process in the present study bore a marked resemblance to that of trabecular bone minerals. These findings are also consistent with previous observation [**49**]. Moreover, nanometer-sized growth twins were clearly visible and the (100) twinning planes are parallel to and running through the length direction of needle-shaped HA single crystals. Interestingly, nanotwins were also found within human apatite crystals, which are believed to affect the adsorption and dissolution properties of the calcified tissues [**50**].

3.3.3. XRD, FT-IR and XPS analysis

Fig. 5(a) shows typical XRD pattern obtained from the surface of Ta-N nanoceramic coatings after immersion in SBF for 14 days. Note that the pattern of natural hydroxyapatite (JCPDS standard no.090432) is also provided for comparison purposes. One set of strong diffraction peaks were found to stem from underlying TaN coatings, while a number of relatively weak and broad peaks can be indexed to HA. The broadening of the peaks suggests that the apatite layers formed on the Ta-N nanoceramic coatings are extremely fine and have low crystallinity. Two strongest diffraction peaks at 2θ values of 25.80 and 31.86 correspond to the (002) and (211) planes of HA, respectively. The intensity ratio of the (002) to (211) peaks is larger than that calculated from reference powder data of JCPDS standard, indicating that the apatite layer has a preferred (002) crystallographic texture. This is consistent with the results of TEM analysis.

Fig. 5(b) presents the FT-IR spectrum obtained from the apatite layers formed on the surface of the Ta-N nanoceramic coatings after immersion in SBF for 14 days. A broad absorption band at the 3000-3700 cm^{-1} range and the bending band at 1659 cm^{-1}, originating from the presence of lattice water in the solid, were observed [**51**], which is a common characteristic of apatite precipitates in aqueous solutions. Two weak shoulder peaks detected at the sites of 3000 and 2850 cm^{-1} can be assigned to ammonium ions [**52**]. The characteristic bands of PO_4^{3-} group were detected at wavenumbers of 1037 and 1090 cm^{-1} for the P-O stretching vibration mode (ν3) and at 603 and 562 cm^{-1} for the O-P-O bending vibrations (ν4) [**53**].The characteristic bands of the CO_3^{2-} group were found at wavenumbers 1455 (ν3), 1421 (ν3), 875 (ν2) and 1545 cm^{-1} (ν3), suggesting that CO_3^{2-} group was incorporated in the apatite lattice. Amongst these, the first three bands

correspond to B-type carbonate-containing apatite, where CO_3^{2-} replaces partial PO_4^{3-} sites in the apatite lattice, and the last band is attributed to A-type carbonate-containing apatite, where CO_3^{2-} substitutes for OH^- sites [**51, 54**]. The absence of the hydroxyl groups represented by stretching (3570 cm^{-1}) and librational (632 cm^{-1}) bands provides further evidence for the existence of A-type carbonate-containing apatite. Therefore, the carbonated hydroxyapatite layers formed on the Ta-N nanoceramic coating after immersion in SBF for 14 days can be confirmed as a mixed AB-type carbonate substitution, akin to natural bone minerals [**55**]. Notably, Ajami [**56**] also observed the formation of an AB-type apatite on the electropolished Ti surface via a biomimetic method in 1.5 SBF.

XPS measurements indicate that Ca, P, O, C and N appear on the surface of the *in vitro* treated Ta-N nanoceramic coating by SBF for 14 days (**Fig. 6(a)**). **Fig. 6(b)-(f)** presents the core level spectra of Ca 2p, P 2p, O 1s, C 1s and N 1s orbitals taken from the hydroxyapatite layer developed on the surface of the Ta-N nanoceramic coatings after immersion of 14 days in SBF. As shown in **Fig. 6(b)**, the Ca 2p spectrum exhibits a doublet with Ca $2p_{3/2}$ and Ca $2p_{1/2}$ peaked at 347.3 and 351.0 eV, corresponding to a divalent oxidation state (Ca^{2+}) in inorganic calcium oxygen compound. The P 2p spectrum shows a single symmetric peak located at 133.8 eV, which can be assigned to P^{5+} state. The measured binding energies for Ca 2p and P 2p are very close to those reported for hydroxyapatite [**57**]. The O 1s spectrum appears as a broad asymmetry peak, which can be well fitted with two components. The component at a binding energy of 531.3 eV may be attributed to a combination of PO_4^{3-}, OH^- and CO_3^{2-} groups. It is difficult to distinguish these groups by peak-fitting routine, due to a negligible chemical shift between them. The other component at a higher binding energy of 532.5 eV signifies the adsorbed water [**58, 59**]. The deconvolution of the C 1s spectrum reveals that the two C1s peaks at 284.8 eV and 286.3 eV correspond to C-C and C-O bonds, respectively, presumably stemming from the carbon contamination on the surface, while the C 1s peak at 287.7 eV represents carbonated group CO_3^{2-} [**41**]. The N 1s spectrum shows a single peak at a binding energy of 400.1 eV, corresponding to the N 1s binding energy of N–H in NH_3 **[60]**.

To shed light on the underlying mechanism that induces apatite deposition, the surface of the *in vitro* treated Ta-N nanoceramic coatings in SBF for 14 days was also examined by removing the precipitated layer (**Fig. 7(a)**). As compared to Ta 4f high resolution spectrum obtained from the

coatings prior to the immersion test (**Fig. 2(a)**), the intensity of the peaks related to the oxynitride phase, TaO_xN_y, rises remarkably for the Ta-N nanoceramic coatings subjected to 14-days immersion in SBF. This observation suggests that during immersion in SBF the surface of the coatings underwent further oxidation.

4. Discussion

The *in vitro* experimental evidence obtained from this work shows that the Ta-N nanoceramic coatings promote apatite formation on Ti-6Al-4V alloy. The hydroxyapatite layers grown on the nanoceramic coatings are homogenous, compact and free of microcracks and delamination. Moreover, they show chemical, morphological and structural properties analogous to those of natural bone minerals. On the basis of these findings, the underlying mechanisms responsible for the remarkable bone-like apatite formation on the Ta-N nanoceramic coatings are discussed here.

Biomimetic apatites developed on the surface of Ta-N coatings in this work are nanocrystalline materials characterized by a high density of interfaces. For example, the volume fraction of interfaces can be as much as 50% for 5 nm grains, 30% for 10 nm grains, and about 3% for 100 nm grains [**61**]. Thus, a substantial fraction of grain boundaries are present on the surface of the material. It would significantly increase surface charge densities and make the surface more reactive than their conventional coarse-grained counterparts, which have grain sizes typically in the range of 100–300 μm [**62**]. Moreover, according to the thermodynamic analysis, the surface or interfacial tension diminishes with decreasing crystal size as a result of the increase in the potential energy of the bulk atoms in the crystals [**63**]. Therefore, smaller crystals with increased molar free energy are more likely to adsorb molecules or ions onto their surfaces in order to decrease the total free energy and to become more stable.

As shown **Fig. 1(a)** and **(b)**, unlike conventional coarse-grained materials utilized for orthopedic implants that have a rather smooth surface at the nanoscale [**64**], the Ta-N nanoceramic coatings possess nanopillar structures on the surface and are 5.8 times rougher than the polished Ti-6Al-4V alloy. Therefore, the Ta-N coatings have more surface area to interact and adsorb ions, promoting apatite nucleation [**65**]. Moreover, according to AFM observations, the average gap between nanopillars is 20.2 nm. This gap is lying within the range between 15 and 50 nm favorable for the adsorption of the Ca and P [**66**].

Based upon the XPS analysis, after immersion of the Ta-N nanoceramic coatings in SBF, an increased amount of TaO_xN_y phase was produced on the surface of the nanoceramic coatings. In addition, a small quantity of NH_3 was present in the hydroxyapatite layer formed on the nanoceramic coatings. Based upon these results, the following hydrolysis reactions were proposed to occur during the immersion of the Ta-N nanoceramic coatings in SBF:

$$Ta\text{-}N + H_2O \rightarrow TaO_xN_y + NH_4^+ + OH^- \quad (1)$$

According to the reaction (1), the partial oxidation of Ta-N coatings in aqueous solution yielded TaO_xN_y and ammonia (NH_3), and subsequently ammonia (NH_3) protonated to form ammonium ions (NH_4^+), thereby increasing local pH value. To clarify the occurrence of reaction (1), the variation of pH value of SBF solution was measured during 7-days soaking of the Ta-N nanoceramic coatings (**Fig. 7(b)**). The measured pH value of SBF solution increased from 7.4 to 7.8 after soaking of 7 days, which validates the reaction (1). It is generally accepted that the electrostatic interaction between the Ca or P ions in the fluid and charged implanted surface is the main driving force for apatite nucleation on the surface [**67**]. The isoelectric point (IEP), defined as the pH at which the surface is electrically neutral, is an important parameter affecting the adsorption properties of implanted materials [**68**]. To date, only isoelectric points of TaON, Ta_2O_5 and Ta_3N_5 relevant to this work have been measured and found to be 2.5, 3.3 and 1.0, respectively [**69**]. Piscanec *et al.* [**70**] attributed the significant bioactivity of TiN-coated hip prosthesis heads to the existence of TiO_xN_y phase formed on the surface of partially oxidized TiN. It is understood that the negative charges provided by the bridging oxygens on the partially oxidized TiN surface promoted the adsorption of Ca^{2+} ions. Therefore, the surface of the Ta-N nanoceramic coatings became negatively charged after soaking in SBF solution with a pH value of 7.4.

Note that negatively-charged surface then selectively adsorbed calcium ions from the solution by Coulomb's force [**71**]. As more and more calcium ions accumulate at the interface between the Ta-N nanoceramic coating and solution, the advancing surface gradually attained an overall positive charge and subsequently combined with negatively charged phosphate ions in SBF solution. When the local supersaturation caused by the enrichment of both calcium and phosphate exceeded the critical level necessary for apatite nucleation, an amorphous calcium phosphate with a low Ca/P atom ratio nucleated and grew by consuming Ca^{2+} and PO_4^{3-} ions from SBF solution [**72**]. Because the amorphous calcium phosphate has a low thermodynamic stability, with the

increase of soaking time this compound crystallized into stable bone-like apatite by incorporating minor ions, such as carbonate and magnesium [**73**]. In addition, as described above, the hydrolysis reaction (1) can release the nitrogen to form ammonium ions, which consumes protons and thereby raises pH value and OH^- concentration of SBF solution. This process increased the supersaturation of the solution with respect to apatite and ionic activity product of the apatite in the fluid, accelerating the rate of apatite formation on the Ta-N nanoceramic coatings [**74**]. **Fig. 8** shows a schematic drawing of the mechanism controlling apatite nucleation on the Ta-N nanoceramic coatings in SBF. By promoting formation of high quality bone-like apatite layers as modelled here, the Ta-N nanoceramic coatings will help realize the potential of Ti alloys as bone implants by addressing some critical aspects of surface robustness and bioactivity.

5. Conclusion

In this work, Ta-N nanoceramic coatings were prepared on Ti–6Al–4V substrates by reactive sputter-deposition using a double glow discharge plasma technique. The sputter-deposited Ta-N coatings are not only ultra-thick (having a thickness of ~30 μm) and adherent, but also extremely dense and homogeneous. They are composed primarily of fcc-TaN phase, which is made of nanocrystallites of about 15–20 nm in diameter, having a strong TaN (200)-oriented texture. After soaking in SBF solution, the formation of bone-like apatite layers on the Ta-N nanoceramic coatings was observed. During the initial stage of apatite precipitation, numerous floccule-like apatite deposits with amorphous structure appeared on the surface, and subsequently, the coating was covered with a homogeneous, compact apatite layer free of microcracks. HRTEM observation indicates that after 14 days of immersion, the precipitated layer consists of needle-like, AB-type apatite crystals with nanotwins, as those found in bone minerals. The mechanism of apatite formation on the Ta-N nanoceramic coatings soaked in SBF solution was modelled. The analysis focuses on the negatively-charged surface of the Ta-N nanoceramic coatings, coupled with surface nanopillar structures. With excellent mechanical robustness and the ability to induce the formation of bone-like apatite layers, the Ta-N nanoceramic coatings should find applicability in the long-term protection and functionalization of bone implant surfaces.

Acknowledgements

The authors acknowledge the financial support of the National Natural Science Foundation of China under Grant No. 51374130 and the Aeronautics Science Foundation of China under Grant No. 2013ZE52058.This work was supported by Funding of Jiangsu Innovation Program for Graduate Education, the Fundamental Research Funds for the Central Universities (CXLX13-151). This study is also supported by the Australian Research Council Discovery Project (DP150102417).

Reference

[1] M. Long and H. J. Rack, *Biomaterials*, 1998, **19**, 1621-1639.

[2] S. E. Pust, D. Scharnweber, C. N. Kirchner and G. Wittstock, *Adv. Mater.*, 2007, **19**, 878-882.

[3] T. Kokubo, *J. Ceram. Soc. Japan*, 1991, **99**, 965-973.

[4] T. Kokubo, *Biomaterials*, 1991, **12**, 155-163.

[5] X. Y. Liu, P. K. Chu and C. X. Ding, *Mater. Sci. Eng. R*, 2004, **47**, 49-121.

[6] A. Fukuda, M. Takemoto, T. Saito, S. Fujibayashi, M. Neo, S. Yamaguchi, T. Kizuki, T. Matsushita, M. Niinomi, T. Kokubo and T. Nakamura, *Acta Biomater.*, 2011, **7**, 1379–1386.

[7] J. P. Landsberg, B. McDonald and F. Watt, *Nature*, 1992, **360**, 65-68.

[8] T. Hanawa, *Mater. Sci. Eng. C*, 2004, **24**, 745-752.

[9] M. Uchida, H.-M. Kim, T. Kokubo, S. Fujibayashi and T. Nakamura, *J. Biomed. Mater. Res.*, 2002, **63**, 522-530.

[10] M. Uchida, A. Oyane, H.-M. Kim, T. Kokubo and A. Ito, *Adv. Mater.*, 2004, **16**, 1071-1074.

[11] X. Bai, S. Sandukas, M. R. Appleford, J. L. Ong and A. Rabiei, *Acta Biomater.*, 2009, **5**, 3563-3572.

[12] M. Hashimoto, K. Kashiwagi and S. Kitaoka, *J. Mater. Sci.: Mater. Med.*, 2011, **22**, 2013–2018.

[13] V.-H. Pham, S.-W. Yook, E-J. Lee, Y. Li, G. Jeon, J.-J. Lee, H.-E. Kim and Y.-H. Koh, *J. Mater. Sci.: Mater. Med.*, 2011, **22**, 2231-2237.

[14] C. Y. Yang, B. C. Wang, E. Chang and B. C. Wu, *J. Mater. Sci.: Mater. Med.*, 1995, **6**, 249-257.

[15] D. K. A. Mann, A. A. Edidin, R. K. Kinoshita and M. T. Manley, *J. Appl. Biomater.*, 1994, **5**, 285-291.

[16] L. Sun, C. C. Berndt, K. A. Gross and A. Kucuk, *J. Biomed. Mater. Res.*, 2001, **58**, 570-592.

[17] H. M. Kim, F. Miyaji, T. Kokubo and T. Nakamura, *J. Mater. Sci.: Mater. Med.*, 1997, **8**, 341-347.

[18] T. Kokubo and S. Yamaguchi, Bioactive Layer Formation on Metals and Polymers. In: P. Ducheyne, editor. Comprehensive Biomaterials. Metallic, Ceramic and Polymeric Biomaterials, Vol. 1. New York: Elsevier; 2011. p. 234-236.

[19] S. Tsukimoto, M. Moriyama and M. Murakami, *Thin Solid Films*, 2004, **460**, 222–226.

[20] Q. Y. Zhang, X. X. Mei, D. Z. Yang, F. X. Chen, T. C. Ma, Y. M. Wang and F. N. Teng, *Nucl. Instrum. Methods Phys. Res. B*, 1997, **127-128**, 664-668.

[21] M. L. Lovejoy, G. A. Patrizi, D. J. Roger and J. C. Barbour, *Thin Solid Films*, 1996, **290-291**, 513-517.

[22] Y. X. Leng, H. Sun, P. Yang, J. Y. Chen, J. Wang, G. J. Wan, N. Huang, X. B. Tian, L. P. Wang and P. K. Chu, *Thin Solid Films*, 2001, **398 –399**, 471–475.

[23] M. H. Ding, B. L. Wang, L. Li and Y. F. Zheng, *Surf. Coat. Technol.*, 2010, **204**, 2519–2526.

[24] B. R. Levine, S. Sporer, R. A. Poggie, C. J. D. Vallea and J. J. Jacobs, *Biomaterials*, 2006, **27**, 4671–4681.

[25] L. L. Liu, J. Xu, P. Munroe, J. K. Xu and Z.-H. Xie, *Acta Biomater.*, 2014, **10**, 1005-1013.

[26] T. Kokubo and H. Takadama, *Biomaterials*, 2006, **27**, 2907-2915.

[27] X. Lu and Y. Leng, *Biomaterials*, 2004, **25**, 1779–1786.

[28] C. Stampfl and A. J. Freeman, *Phys. Rev. B*, 2005, **71**, 024111.

[29] P. H. Mayrhofer, C. Mitterer, L. Hultman and H. Clemens, *Prog. Mater. Sci.*, 2006, **51**, 1032–1114.

[30] P. Losbichler and C. Mitterer, *Surf. Coat. Technol.*, 1997, **97**, 567–573.

[31] Y.Cheng, W. Cai, H. T. Li, Y. F. Zheng and L. C. Zhao, *Surf. Coat. Technol.*, 2004, **186**, 346-352.

[32] D. de F. Aplicada, F. de Ciencias, C-XII and U.A. de Madrid, *Appl. Phys. A*, 2005, **81**, 1405-1410.

[33] P. Lamour, P. Fioux, A. Ponche, M. Nardin, M.-F. Vallat, P. Dugay, J.-P. Brun, N. Moreaud and J.-M. Pinvidic, *Surf. Interface Anal.*, 2008, **40**, 1430-1437.

[34] Z. Wang, O. Yaegashi, H. Sakaue, T. Takahagi and S. Shingubara, *J. Appl. Phys.*, 2003, **94**,

4697-4701.

[35] L. P. B. Lima, J. A. Diniz, I. Doi, J. Miyoshi,A. R. Silva and J. G. Fo, *J. Vac. Sci. Technol. B*, 2012, **30**, 042202.

[36] Z. X. Zhang, H. Dong and T. Bell, *Surf. Coat. Technol.*, 2006, **200**, 5237-5244.

[37] X. Ma and A. Matthews, *Surf. Coat. Technol.*, 2007, **202**, 1214-1220.

[38] Z. Chen, L. Y. L. Wu, E. Chwa and O. Tham, *Mater. Sci. Eng. A*, 2008, **493**, 292-298.

[39] S. Hogmark, S. Jacobson and M. Larsson, *Wear*, 2000, **246**, 20-33.

[40] A. Mihranyan, J. Forsgren, M. StrΦmme and H. Engqvist, *Langmuir*, 2009, **25**, 1292-1295.

[41] Y. W. Gu, K. A. Khor, D. Pan and P. Cheang, *Biomaterials*, 2004, **25**, 3177-3185.

[42] S. R. Paital and N. B. Dahotre, *Acta Biomater.*, 2009, **5**, 2763-2772.

[43] X. Zhou, R. Siman, L. Lu and P. Mohanty, *Surf. Coat. Technol.*, 2012, **207**, 343-349.

[44] S. Jalota, S. Bhaduri and S. B. Bhaduri, *J. Mater. Res.*, 2007, **22**, 1593-1600.

[45] H. Takadama, H.-M. Kim, T. Kokubo and T. Nakamura, *Chem. Mater.*, 2001, **13**, 1108-1113.

[46] E. D. Eanes, J. D. Termine and M. U. Nylen, *Calc. Tiss. Res.*, 1973, **12**, 143-158.

[47] Y.-F. Chou, W.-A. Chiou, Y. Xu, J. C. Y. Dunn and B. M. Wu, *Biomaterials*, 2004, **25**, 5323-5331.

[48] M. Aizawa, A. E. Porter, S. M. Best and W. Bonfield, *Biomaterials*, 2005, **26**, 3427-3433.

[49] S. I. Hong, K. H. Lee, M. E. Outslay and D. H. Kohn, *J. Mater. Res.*, 2008, **23**, 478-485.

[50] E. F. Bres, W. G. Waddington, J.-C. Voegel, J. C. Barry and R. M. Frank, *Biophys. J.*, 1986, **50**, 1185-1193.

[51] A. Roguska, M. Pisarek, M. Andrzejczuk, M. Dolata, M. Lewandowska and M. Janik-Czachor, *Mater. Sci. Eng. C*, 2011, **31**, 906-914.

[52] G. Ramis, L. Yi and G. Busca, *Catal. Today*, 1996, **28**, 373-380.

[53] C. C. Ribeiro, I. Gibson and M. A. Barbosa, *Biomaterials*, 2006, **27**, 1749-1761.

[54] L. Müller and F. A. Müller, *Acta Biomater.*, 2006, **2**, 181-189.

[55] C. Rey, B. Collins, T. Goehl, I. R. Dickson and M. J. Glimcher, *Calcif. Tissue Int.*, 1989, **45**, 157–164.

[56] E. Ajami and K. F. Aguey-Zinsou, *J. Funct. Biomater.*, 2012, **3**, 327-348.

[57] B.-H. Lee, Y. D. Kim and K. H. Lee, *Biomaterials*, 2003, **24**, 2257-2266.

[58] J. Kunze, L. Müller, Jan M. Macak, P. Greil, P. Schmuki and F. A. Müller, *Electrochim. Acta*,

2008, **53**, 6995-7003.

[59] M. A. Baker, S. L. Assis, O. Z. Higa and I. Costa, *Acta Biomater.*, 2009, **5**, 63-75.

[60] H. Y. Ha, H. J. Jang, H. S. Kwon and S. J. Kim, *Corros. Sci.*, 2009, **51**, 48-53.

[61] M. A. Meyers, A. Mishra and D. J. Benson, *Prog. Mater. Sci.*, 2006, **51**, 427–556.

[62] V. Guidi, M. C. Carotta, M. Ferroni, G. Martinelli, L. P aglialonga, P. Nelli and G. Sberv eglieri, Nanophase metals. Proceedings of the 12th European Conference on Solid-State Tranducers and the 9th UK Conference on Sensors and their Applications, 1999, **1**, 501.

[63] H. Zhang, R. L. Penn, R. J. Hamers and J. F. Banfield, *J. Phys. Chem. B*, 1999, **103**, 4656–4662.

[64] F. S. Kaplan, W. C. Lee, T. M. Keaveny, A. Boskey, T. A. Einhorn and J. P. Iannotti, Form and function of bone. In: Simon SP, editor. Orthopedic basic science. Columbus, OH: American Academy of Orthopedic Surgeons, 1994, p. 127–85.

[65] C.-M. Lin and S.-K. Yen, *Mater. Sci. Eng. C*, 2006, **26**, 54-64.

[66] T. Peltola, M. Jokinen, H. Rahiala, M. Pätsi, J. Heikkilä, I. Kangasniemi and A. Yli-Urpo, *J. Biomed. Mater. Res.*, 2000, **51**, 200-208.

[67] Y. T. Xie, X. Y. Liu, P. K. Chu and C. X. Ding, *Surf. Sci.*, 2006, **600**, 651–656.

[68] G. A. Parks and P. L. de Bruyn, *J. Phys. Chem.*, 1961, **66**, 967–973.

[69] W.-J. Chun, A. Ishikawa, H. Fujisawa, T. Takata, J. N. Kondo, M. Hara, M. Kawai, Y. Matsumoto and K. Domen, *J. Phys. Chem. B*, 2003, **107**, 1798-1803.

[70] S. Piscanec, L. C. Ciacchi, E. Vesselli, G. Comelli, O. Sbaizero, S. Meriani and A. D. Vita, *Acta Mater.*, 2004, **52**, 1237-1245.

[71] X. Y. Liu, A. P. Huang, C. X. Ding and P. K. Chu, *Biomaterials*, 2006, **27**, 3904-3911.

[72] X.-B. Chen, Y.-C. Li, P. D. Hodgson and C. Wen, *Acta Biomater.*, 2009, **5**, 2290-2302.

[73] X. Y. Liu, C. X. Ding and P. K. Chu, *Biomaterials*, 2004, **25**, 1755-1761.

[74] L. Jonásová, F. A. Müller, A. Helebrant, J. Strnad and P. Greil, *Biomaterials*, 2004, **25**, 1187–1194.

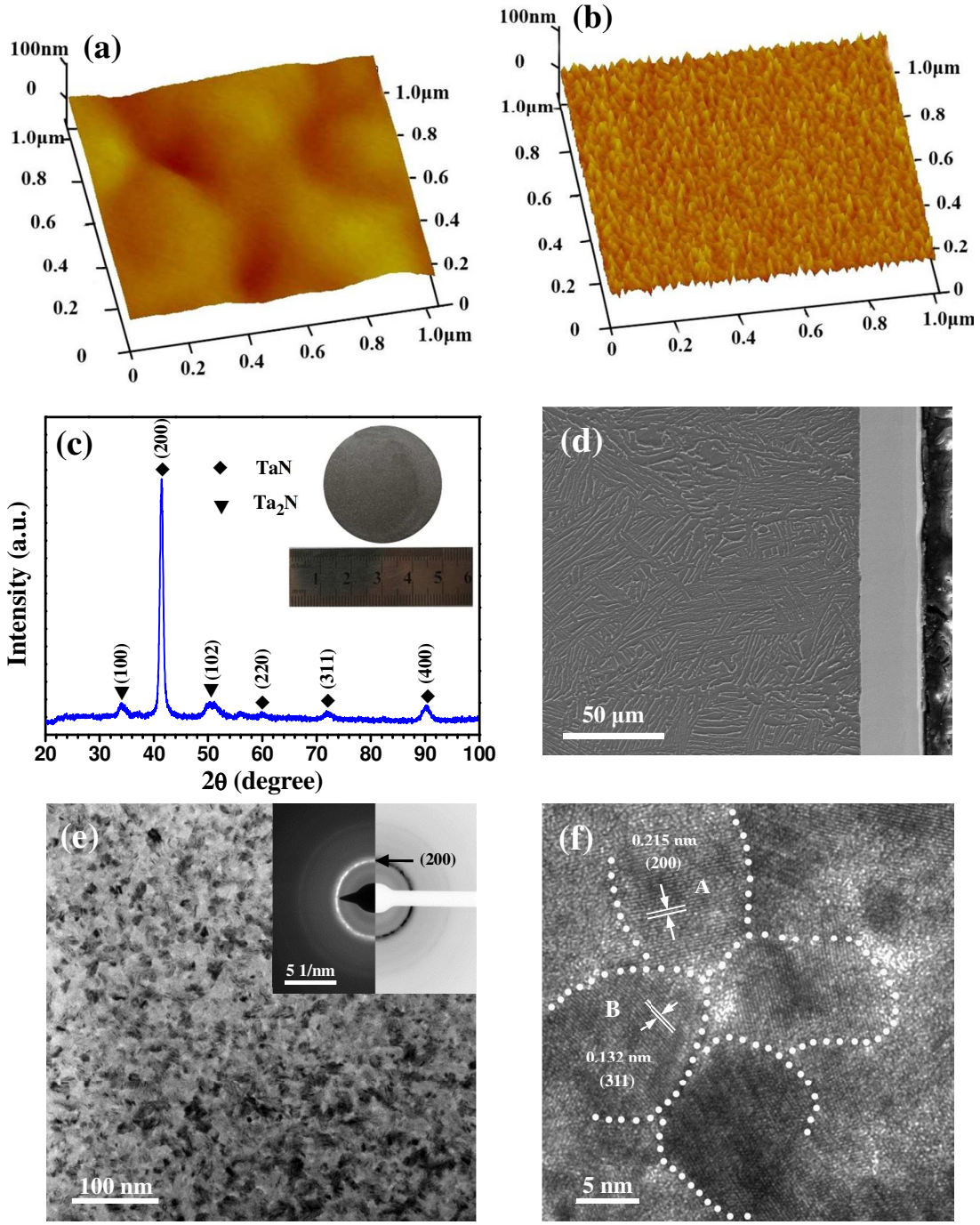

Fig. 1 AFM surface morphology of the polished Ti-6Al-4V alloy (a) before and (b) after sputter deposition of Ta-N layer; (c) XRD pattern and (d) FE-SEM cross-sectional morphology of the Ta-N coating prepared onto Ti-6Al-4V alloy; (e) TEM bright field image and corresponding SAED pattern of the Ta-N coating; (f) high-resolution TEM image of the Ta-N coating.

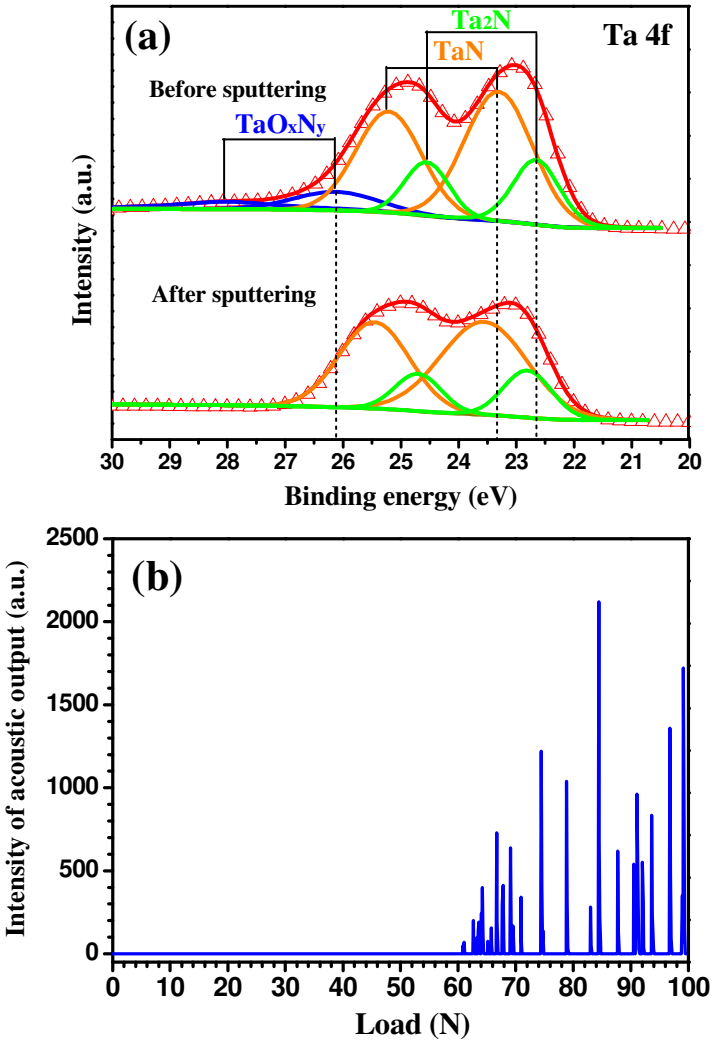

Fig. 2 (a) Ta 4f core-level spectra recorded from the as-deposited Ta-N coating before and after 10 min of sputtering with a 4.5 kV Ar^+ ion beam; (b) Acoustic emission curve vs. normal load for the as-deposited Ta-N coating.

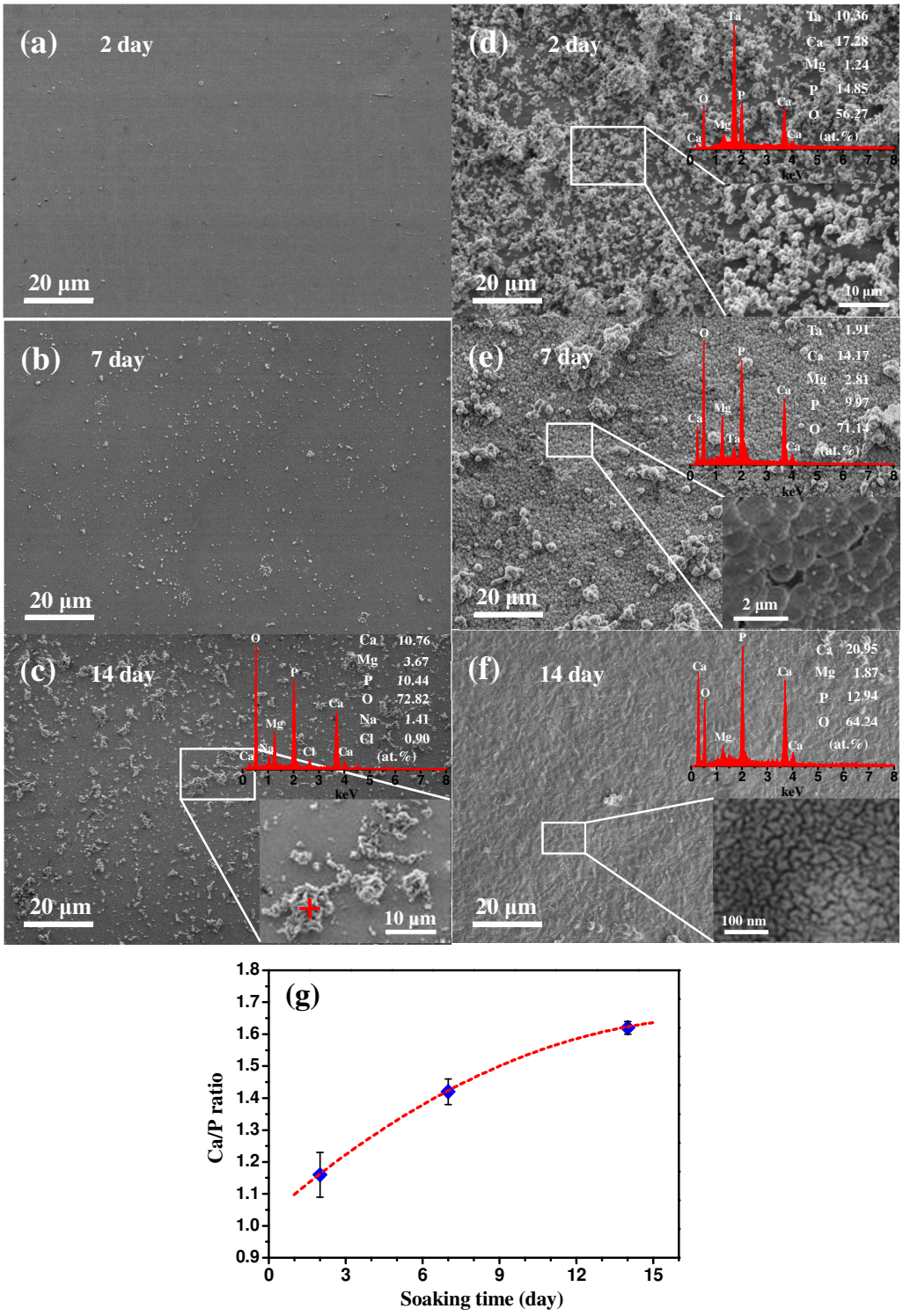

Fig. 3 SEM surface micrographs of (a-c) uncoated and (d-f) Ta-N coated Ti-6Al-4V alloys after soaking in SBF for various periods and (g) the Ca/P ratio in the precipitated layers on the Ta-N coating as a function of soaking time in SBF. The lower right insets in (c)-(f) show higher magnification images of selected areas, and the upper right insets in (c)-(f) shows EDS spectrum taken from region marked by "+".

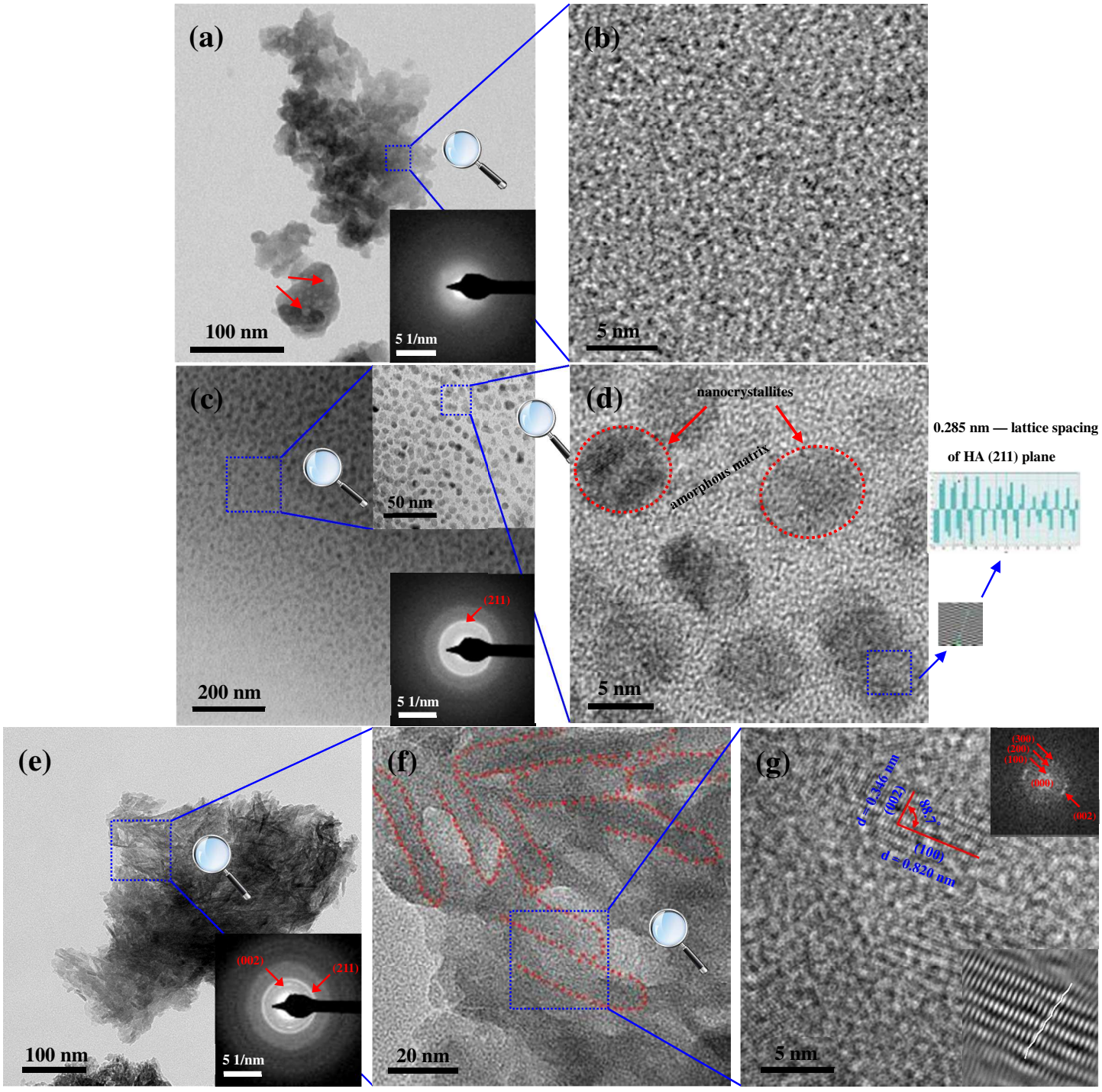

Fig. 4 TEM bright field image and the corresponding HRTEM images of the precipitated layer after (a, b) 2, (c, d) 7 and (e-f) 14 days of soaking in SBF. The lower right insets in (a, c, e) show the SAED pattern, The upper right inset in (c) show higher magnification images of selected areas, and the upper right and lower right insets in (g) show the FFT pattern and processed higher magnification image of needle-shaped apatite crystal, respectively.

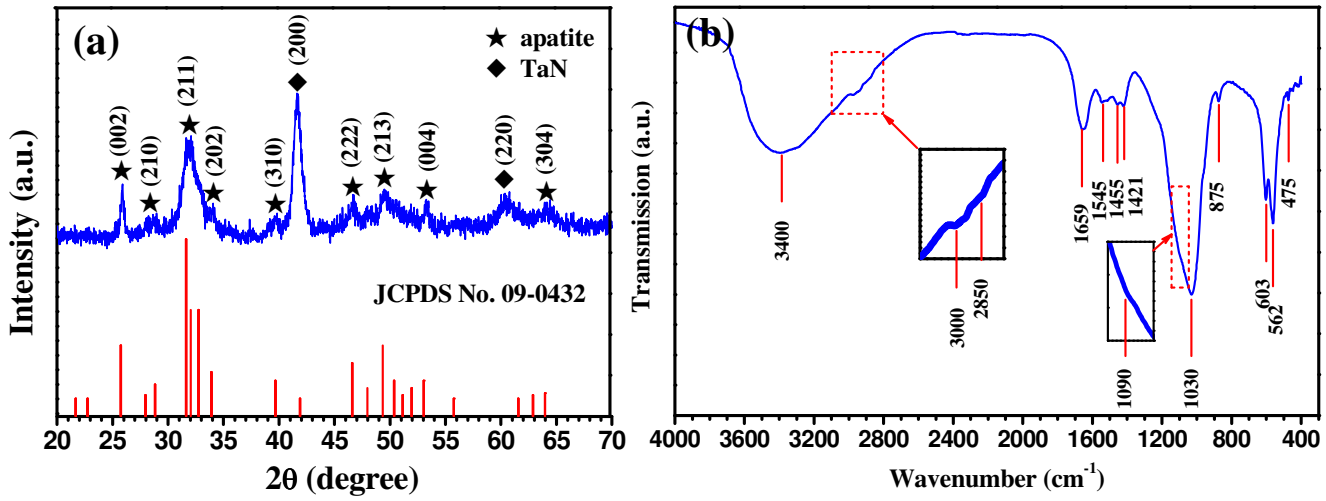

Fig. 5 (a) Comparison of XRD pattern obtained from the Ta-N coating after immersion in SBF for 14 days and the pattern of natural hydroxyapatite (JCPDS standard no.090432); (b) FT-IR spectrum of the biomimetic apatite layer on the surface of the Ta-N coating after immersion in SBF for 14 days.

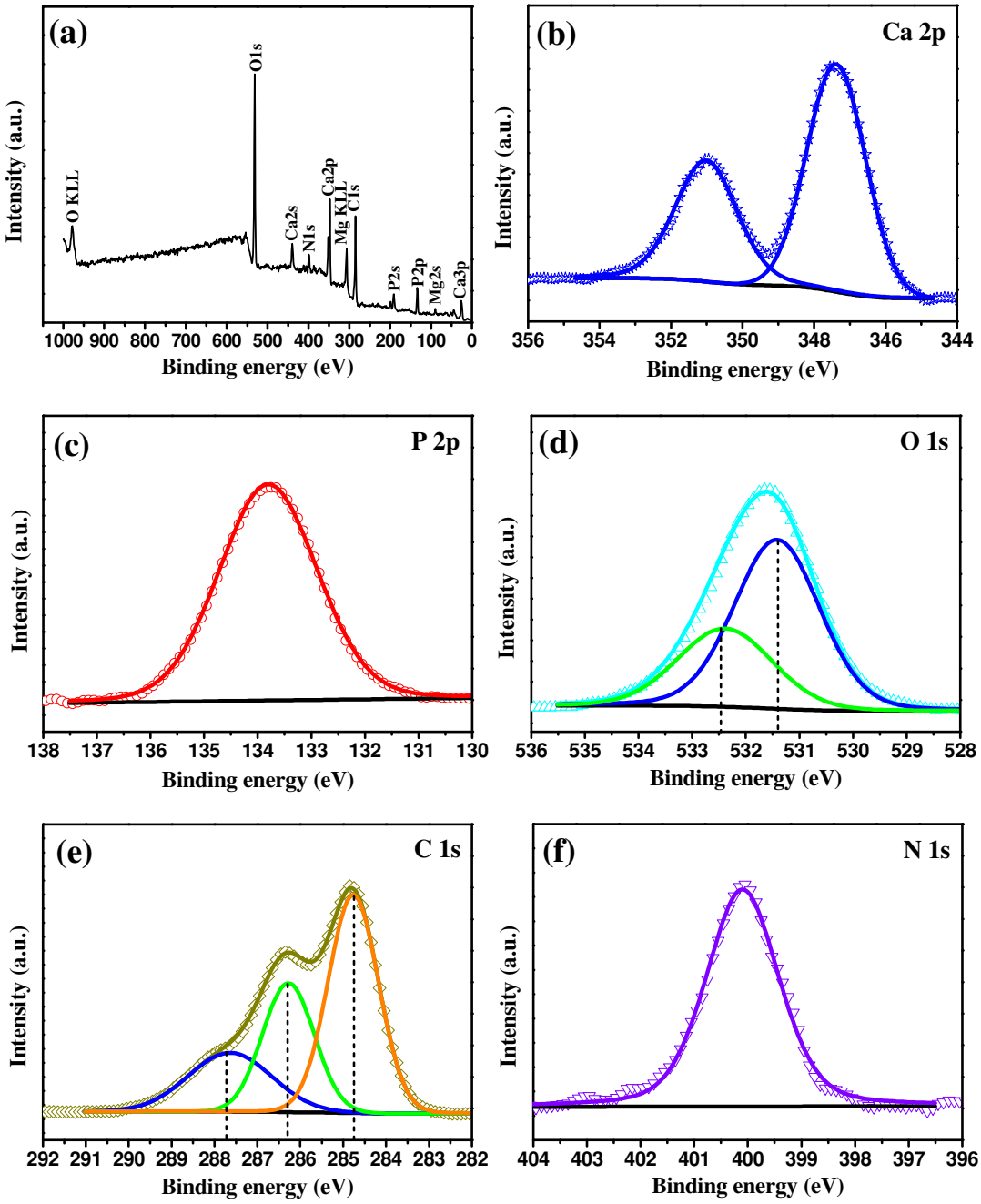

Fig. 6 (a) XPS survey spectrum and the core level spectra of (b) Ca 2p, (c) P 2p, (d) O 1s, (e) C 1s and (f) N1s taken form the biomimetic apatite layer on the surface of the Ta-N coating after immersion in SBF for 14 days.

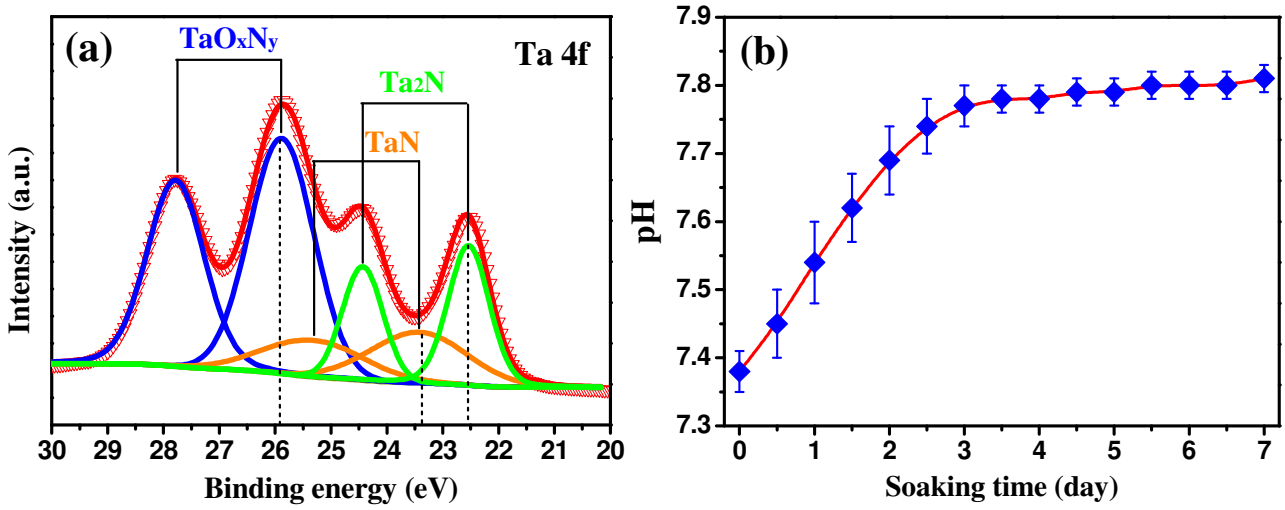

Fig. 7 (a) Ta 4f core-level spectrum recorded from the surface of the in vitro treated Ta-N nanoceramic coating immersed in SBF for 14 days after scraping off the precipitated layer; (b) variation of pH value of SBF solution during soaking of the Ta-N nanoceramic coating for 7 days.

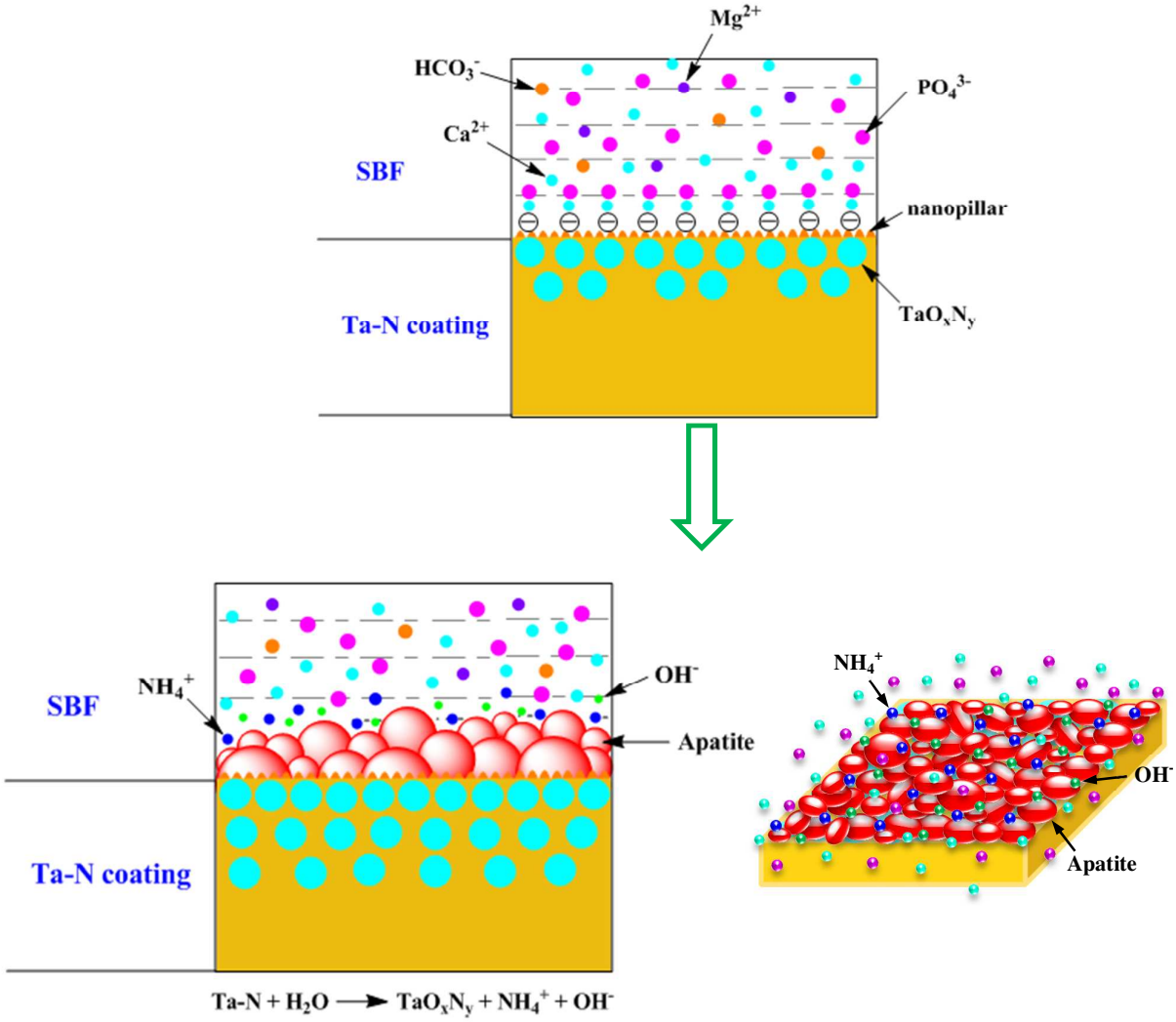

Fig. 8 Schematic illustration of apatite nucleation and growth on the Ta-N nanoceramic coating soaked in SBF.